EES Catalysis

PAPER

View Article Online
View Journal | View Issue

Cite this: *EES Catal.*, 2023, 1, 552

Electron-rich pyrimidine rings enabling crystalline carbon nitride for high-efficiency photocatalytic hydrogen evolution coupled with benzyl alcohol selective oxidation†

Zhi Lin,[a] Yiqing Wang,[a] Ta Thi Thuy Nga,[b] Jie Zhang,[c] Ruizhe Wang,[a] Zhengqi Zhang,[a] Yufei Xu,[a] Daming Zhao,[d] Chung-Li Dong[b] and Shaohua Shen*[a]

Photocatalytic water splitting over polymeric carbon nitride (PCN) has been seriously limited by the poor charge carrier transfer ability and sluggish four-electron water oxidation kinetics. Herein, crystalline carbon nitride (CCN-Pr) with electron-rich pyrimidine rings introduced in the molecular structure is synthesized by a two-step self-assembly and molten-salt annealing strategy for photocatalytic hydrogen evolution coupled with benzyl alcohol selective oxidation to benzaldehyde, instead of the kinetically sluggish water oxidation reaction. Owing to the synergistically tuned band and electronic structures, the obtained CCN-Pr exhibits excellent photocatalytic performances, with the highest hydrogen and benzaldehyde production rates reaching 149.39 μmol h^{-1} and 154.62 μmol h^{-1}, respectively. The apparent quantum yield for hydrogen evolution is determined to be 20.27% at 420 nm, encouragingly standing at the highest level reported for simultaneous hydrogen and benzaldehyde production over PCN-based photocatalysts. It is well evidenced that the introduced electron-rich pyrimidine rings could finely tune the band structures for extended optical absorption and matched redox potentials for water reduction and benzyl alcohol oxidation. Theoretical calculation and experimental results reveal that the electronic structure engineered by pyrimidine rings alters the charge density distribution for promoted charge transport, and creates abundant reactive sites to accelerate the surface oxidation reaction kinetics. This work provides a reliable strategy to design efficient photocatalysts with band and electronic structures engineered by the tunable molecular structures, and also paves an alternative way to promote the economic benefits and the technology upgrading of solar energy conversion and utilization.

Received 12th March 2023,
Accepted 24th April 2023

DOI: 10.1039/d3ey00055a

rsc.li/eescatalysis

Broader context

Photocatalytic water splitting for hydrogen production has been considered a promising technology to convert solar energy to chemical energy *via* zero-carbon cycle. However, the overall water splitting performance is still far from satisfactory, as it is mainly limited by the sluggish kinetics and endergonic thermodynamics of the water oxidation reaction. Moreover, oxygen production *via* photocatalytic water splitting is not economically and technically competitive, given the fact that oxygen could be easily produced on a large scale *via* simple air distillation process. Herein, crystalline PCN with electron-rich pyrimidine rings introduced in the molecular structure is used for photocatalytic hydrogen evolution coupled with benzyl alcohol selective oxidation to benzaldehyde, instead of the kinetically sluggish water oxidation reaction. It is well evidenced that the synergistic effects contributed from the tuned band and electronic structures give rise to the remarkable enhancement in photocatalytic benzyl alcohol oxidation and hydrogen evolution over PCN with molecular structures rationally engineered *via* the introduction of electron-rich pyrimidine rings. This work provides a reliable strategy to design efficient photocatalysts with band and electronic structures engineered by the tunable molecular structures, and also paves an alternative way to promote the economic benefits and technology upgrade of solar energy conversion and utilization.

[a] *International Research Center for Renewable Energy, State Key Laboratory of Multiphase Flow in Power Engineering, Xi'an Jiaotong University, Shaanxi, 710049, China. E-mail: shshen_xjtu@mail.xjtu.edu.cn*
[b] *Department of Physics, Tamkang University, New Taipei City, 25137, Taiwan*
[c] *School of Civil and Architecture Engineering, Xi'an Technological University, Xi'an 710021, China*
[d] *School of Advanced Energy, Shenzhen Campus of Sun Yat-sen University, Shenzhen 518107, China*

† Electronic supplementary information (ESI) available. See DOI: https://doi.org/10.1039/d3ey00055a

Introduction

Photocatalytic water splitting to produce hydrogen and oxygen is thought to be a promising and sustainable approach for solar energy conversion *via* zero-carbon cycle, which is expected to reduce the world's dependence on fossil fuels.[1,2] The key to efficiently converting solar energy into hydrogen energy *via* photocatalytic water splitting is to develop stable, high-performance, and low-cost photocatalysts.[3] Except for various metal-based semiconducting photocatalysts, polymeric carbon nitride (PCN), as a visible-responsive, inexpensive, nontoxic, and stable conjugated polymer semiconductor, has attracted much research attention and been extensively explored for photocatalysis in past years.[4] Nevertheless, the fast charge carrier recombination, sluggish surface reaction kinetics, and the narrow visible photoresponse range largely limit its photocatalytic activity for water splitting.[5] To overcome these drawbacks, many effective attempts have been proposed to improve the photocatalytic activity of PCN, including crystal structure engineering,[6,7] element doping,[8] morphology tuning,[9,10] heterostructure construction,[11–13] and single metal atom loading.[14,15] Based on boron-doped and nitrogen-deficient PCN nanosheets, Shen *et al.* designed an all-PCN based 2D/2D Z-scheme heterojunction for efficient photocatalytic overall water splitting.[16] Benefiting from the strong interfacial interaction, the matched band structure, and ultrathin nanostructures, this Z-scheme heterojunction received a solar-to-hydrogen (STH) efficiency as high as 1.16%. However, one should be aware that the overall water splitting performance is still far from satisfactory, as it is mainly limited by the water oxidation reaction with sluggish kinetics and endergonic thermodynamics.[17] Moreover, oxygen production *via* photocatalytic water splitting is not economically and technically competitive, given the fact that oxygen could be easily produced on a large scale *via* simple air distillation process.[18] Alternatively, oxidative synthesis of value-added organics that couples with hydrogen evolution could be expectedly more viable and valuable, with both photocatalytic efficiency and product value much improved, as compared to the photocatalytic water splitting system for simultaneous hydrogen and oxygen production.

In the photoredox-catalyzed coupling reaction system, the organic substrate oxidation reaction would be much more kinetically favored than the four-electron process for oxygen production, accompanying the great enhancement in hydrogen evolution activity.[19] Moreover, the value-added oxidative products generated by the coupled photocatalytic reactions could be widely used as fine chemicals with large economic benefits.[20] As an essential industrial raw material, benzaldehyde obtained from the oxidation of benzyl alcohol is an important intermediate for the synthesis of herbicides, pharmaceuticals, and perfumes.[21] However, the conventional oxidation method for benzaldehyde production requires hazardous oxidants (*e.g.*, $K_2Cr_2O_7$, V_2O_5, and $KMnO_4$), with the oxidation reactions always occurring at high temperature and high pressure,[22] which would inevitably increase production costs and cause environmental pollution. Thus, selective oxidation of benzyl alcohol to benzaldehyde by photocatalysis, along with efficient hydrogen production *via* water reduction, would be of great promise in industry and has made noticeable advances in recent years. For example, by introducing L-arginine into the molecular structure, Fu *et al.* prepared a PCN photocatalyst with adjustable bandgaps and achieved excellent photocatalytic performances for water reduction and benzyl alcohol oxidation to benzaldehyde,[23] with the hydrogen evolution rate reaching 95.3 μmol h^{-1} and benzaldehyde production selectivity achieving 99.7%. Moreover, it has been proven to be effective to enhance the photocatalytic activity for hydrogen evolution coupled with benzyl alcohol selective oxidation, with the charge carrier separation and reaction kinetics accelerated by improving the crystallinity of PCN. By using NaCl as the ion-induction agent, Huo *et al.* prepared high crystallinity Na^+-doped PCN nanosheets with altered charge density distribution,[24] which exhibited facilitated charge transfer processes and rapid surface reaction kinetics, thus significantly improving the photocatalytic activity for hydrogen evolution and benzyl alcohol oxidation, with the apparent quantum yield reaching 10.5% at 420 nm. Based on these observations, it is expected that efficient photocatalysts for hydrogen evolution coupled with benzyl alcohol selective oxidation could be well-designed by tuning the band and electronic structures of crystalline PCN.

Herein, high crystalline PCN with electron-rich pyrimidine rings introduced into the molecular structure (CCN-Pr) was synthesized through a two-step self-assembly and molten-salt annealing strategy for the photocatalytic hydrogen evolution coupled with the selective oxidation of benzyl alcohol to benzaldehyde. With molecular structures altered by the introduced pyrimidine rings, excellent performances for the hydrogen evolution and selective oxidation of benzyl alcohol to benzaldehyde (conversion: 91%, selectivity: 99%, at 12 h) could be realized over the obtained CCN-Pr photocatalysts, with the hydrogen and benzaldehyde evolution rates reaching 149.39 and 154.62 μmol h^{-1}, respectively, which stands at the highest level reported for PCN-based photocatalysts. Experimental and theoretical studies have shown that the introduced electron-rich pyrimidine rings could finely tune the band structures for the extended optical absorption and the matched redox potentials for water reduction and benzyl alcohol oxidation reactions, as well as modulate the electronic structures, thus altering the charge density distribution for the promoted charge carrier separation and transfer. Moreover, the C atoms in the introduced pyrimidine rings could serve as the reactive sites for the rapid adsorption of benzyl alcohol and desorption of benzaldehyde, and then accelerate the surface oxidation reaction kinetics.

Results and discussion

Herein, CCN-Pr with tunable molecular structures is synthesized through a two-step self-assembly and molten-salt annealing strategy (see Experimental section for details in ESI†). As illustrated in Fig. 1a, with 2,4,6-triaminepyrimidine (TAP), melamine and cyanuric acid self-assembled into the supramolecular

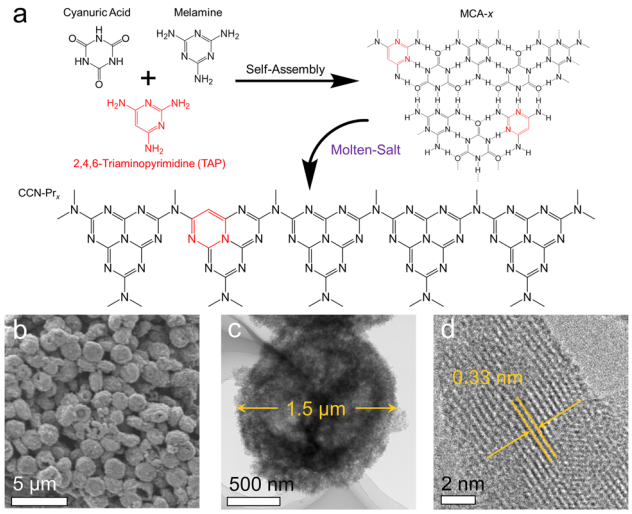

Fig. 1 (a) The proposed preparation process of CCN-Pr$_x$. (b) Scanning electron microscopy (SEM) and (c and d) transmission electron microscopy (TEM) images of CCN-Pr$_{40}$.

precursors (MCA-x, x = 0, 20, 40, 60, 80), where x represents the feeding amounts (mg) of TAP in precursors, the CCN-Pr$_x$ photocatalysts with pyrimidine rings introduced into the molecular structure could be obtained by annealing the MCA-x precursors in KCl/LiCl molten salts. The obtained CCN-Pr$_x$ spheres (taking CCN-Pr$_{40}$ as the example) with an average diameter of ~1.5 μm (Fig. 1b and c) present high crystallinity, as identified by the clear lattice spacing of 0.33 nm (Fig. 1d), owing to the liquid-phase reaction environment provided by the KCl/LiCl molten salts that reduce the kinetic obstacles for the improved crystallinity.[25] In comparison, without the KCl/LiCl molten salts during annealing, the obtained PCN sample (CN) with similar spherical morphology (Fig. S1a, ESI†) reveals an amorphous structure (Fig. S1b, ESI†). This demonstrates the necessity of molten salts for the crystallization of the annealing synthesized PCN, which is further supported by X-ray diffraction (XRD) analysis. As shown in Fig. 2a, the amorphous CN synthesized in the absence of KCl/LiCl molten salts during annealing presents two distinct XRD peaks at 2θ = 13.1° and 27.1°, assigned to the (100) and (002) planes of PCN, respectively. In comparison, all of the CCN-Pr$_x$ samples synthesized in the presence of molten salts present very similar XRD patterns, with (100) and (002) peaks shifted to 2θ = 8.0° and 27.9°, respectively, indicating the reduced interlayer distance and the condensed in-plane conjugated skeleton for CCN-Pr$_x$ with high crystallinity.[25] The narrowed full width at half-maximum (FWHM) observed for the (002) peaks of CCN-Pr$_x$ also evidences the improved crystallinity induced by molten-salt annealing (Table S1, ESI†).[26]

Depending on the introduction of pyrimidine rings, the molecular structure evolution was then investigated over the obtained CCN-Pr$_x$ photocatalysts. Elemental analysis reveals the gradually increased carbon contents in CCN-Pr$_x$ with the increasing amounts of TAP introduced in the supramolecular precursors (Table S2, ESI†), suggesting the successful incorporation of pyrimidine rings into the PCN framework. Fourier transform infrared (FT-IR) spectra (Fig. 2b) show very similar fingerprint signals for all of the CCN-Pr$_x$ photocatalysts, with the peaks at 1200–1700 cm^{-1}, ~810 cm^{-1} and 3000–3500 cm^{-1} attributed to the skeletal vibration of heptazine rings, the out-of-plane bending of heptazine rings, and the stretching vibrations of –NH$_2$ and –NH–, respectively.[27] These similar FT-IR fingerprints suggest that the introduction of pyrimidine rings would not remarkably change the original heptazine units in CCN-Pr$_x$.[28] By further looking into the atomic structures

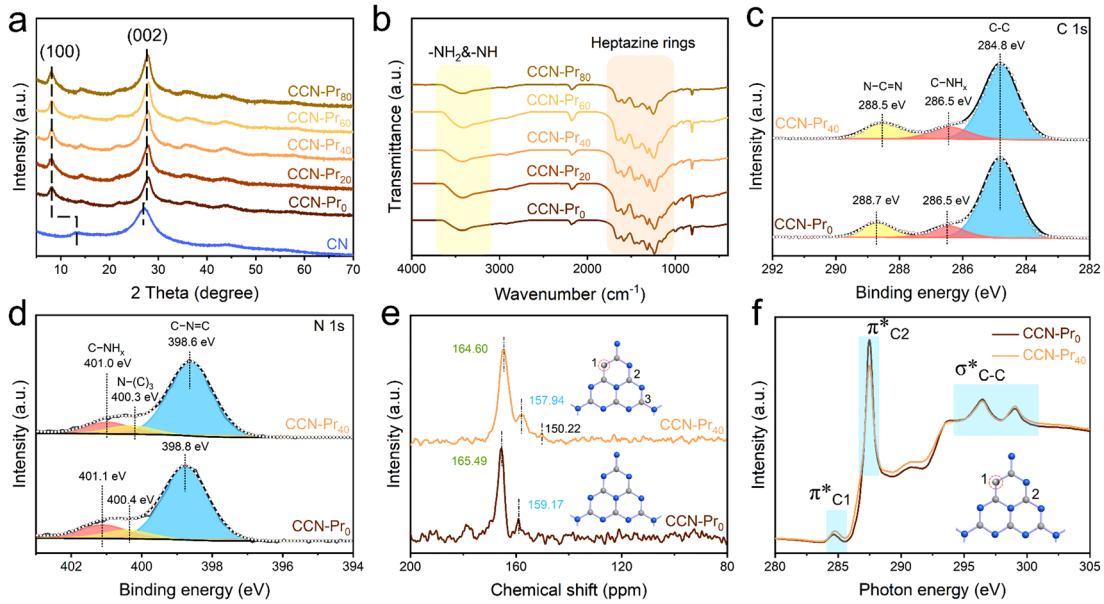

Fig. 2 (a) XRD patterns of CN and CCN-Pr$_x$. (b) FT-IR spectra of CCN-Pr$_x$. High-resolution XPS spectra of (c) C 1s and (d) N 1s for CCN-Pr$_0$ and CCN-Pr$_{40}$. (e) Solid-state ^{13}C CP-NMR and (f) C K-edge XANES spectra of CCN-Pr$_0$ and CCN-Pr$_{40}$. Gray: C, blue: N.

monitored by X-ray photoelectron spectroscopy (XPS), one would note that the high-resolution XPS C 1s spectrum could be deconvoluted into three peaks at 284.8, 286.5, and 288.7 eV for CCN-Pr_0 (Fig. 2c), corresponding to the adventitious carbon (C–C), the C–NH_x groups, and the N–C═N units in PCN framework, respectively.[29] In comparison, the peak assigned to the N–C═N units is slightly shifted to lower binding energy for CCN-Pr_{40}, which verifies the possible replacement of N atoms in heptazine rings by C atoms with low electronegativity.[30] It is also noted that the three distinct XPS N 1s peaks (Fig. 2d) corresponding to the C–N═C, N–$(C)_3$, and C–NH_x groups[31] are slightly shifted to lower binding energy for CCN-Pr_{40} relative to CCN-Pr_0, suggesting that the introduced electron-rich pyrimidine rings would increase the electron density of N atoms.[30] Solid-state ^{13}C cross-polarization nuclear magnetic resonance (CP-NMR) spectra (Fig. 2e) further identify two strong peaks at 165.49 and 159.17 ppm for CCN-Pr_0, which should be derived from the C atoms in the C–N_3 and CN_2–(NH_x) groups, respectively, confirming the heptazine structures in CCN-Pr_0.[32] In comparison, these two peaks are slightly shifted to 164.60 and 157.94 ppm, respectively, for CCN-Pr_{40}, indicating that CCN-Pr_{40} maintains the heptazine framework, but the electron density is disturbed by the introduced electron-rich pyrimidine rings. An additional peak could be observed at 150.22 ppm for CCN-Pr_{40}, belonging to the C atoms in the sp^2 C═C electron-withdrawing group in pyrimidine rings,[33] which evidences the introduction of pyrimidine rings into the PCN skeleton, as further confirmed by the C K-edge X-ray absorption near edge structure (XANES) spectra (Fig. 2f). The peaks at 284.7, 287.5 and 294.4–301.7 eV should be attributed to the orbital transition of $\pi^*_{C=C}$ (π^*_{C1}), $\pi^*_{C-N=C}$ (π^*_{C2}) and σ^*_{C-C}, respectively. The doublet peaks at 294.4–301.7 eV, featured for crystalline PCN, are observed in both CCN-Pr_0 and CCN-Pr_{40} with high crystallinity.[34] The π^*_{C1} peak intensity is increased for CCN-Pr_{40}, relative to CCN-Pr_0, which is attributed to the successful introduction of pyrimidine rings with C═C bonds into CCN-Pr_{40}.[35] Furthermore, the significantly reduced π^*_{C2} peak intensity indicates that some of the empty orbitals in the heptazine units are filled with electrons provided by the electron-rich pyrimidine rings.[36] These spectral variations evidence that the introduced pyrimidine rings would induce the charge density redistribution in the obtained CCN-Pr_{40}.

All of the above molecular and atomic structural analyses confirm the successful introduction of electron-rich pyrimidine rings into CCN-Pr_x. Depending on the increasing TAP feeding amounts, the obtained CCN-Pr_x photocatalysts exhibit a progressive redshift in the optical absorption edges (Fig. 3a), with the bandgap (E_g) gradually narrowed from 2.43 eV for CCN-Pr_0 to 1.49 eV for CCN-Pr_{80} (Fig. 3b). Given the very close conduction band (CB) and flat band potentials for a typical n-type semiconductor, the CB potentials (E_c) could be determined from the Mott–Schottky plots for CCN-Pr_x, cathodically shifted from −0.47 V (*vs.* reversible hydrogen electrode, RHE) for CCN-Pr_0 to −0.73 V (*vs.* RHE) for CCN-Pr_{80} (Fig. 3c). Then, the valence band (VB) potentials (E_v), calculated by E_g and E_c (see Fig. S2 and related discussion in ESI†),[37] are cathodically shifted from 1.96 V (*vs.* RHE) for CCN-Pr_0 to 0.76 V (*vs.* RHE) for CCN-Pr_{80}, depending on the increasing TAP feeding amounts (Fig. 3d). It is thus convincing that the introduction of pyrimidine rings could rationally engineer the band structures of CCN-Pr_x, with the CB and VB positions finely tuned to broaden the optical absorption region and match the redox potentials for the water reduction and benzyl alcohol oxidation reactions.[38]

To further understand the electronic structure evolution with the introduction of electron-rich pyrimidine rings,

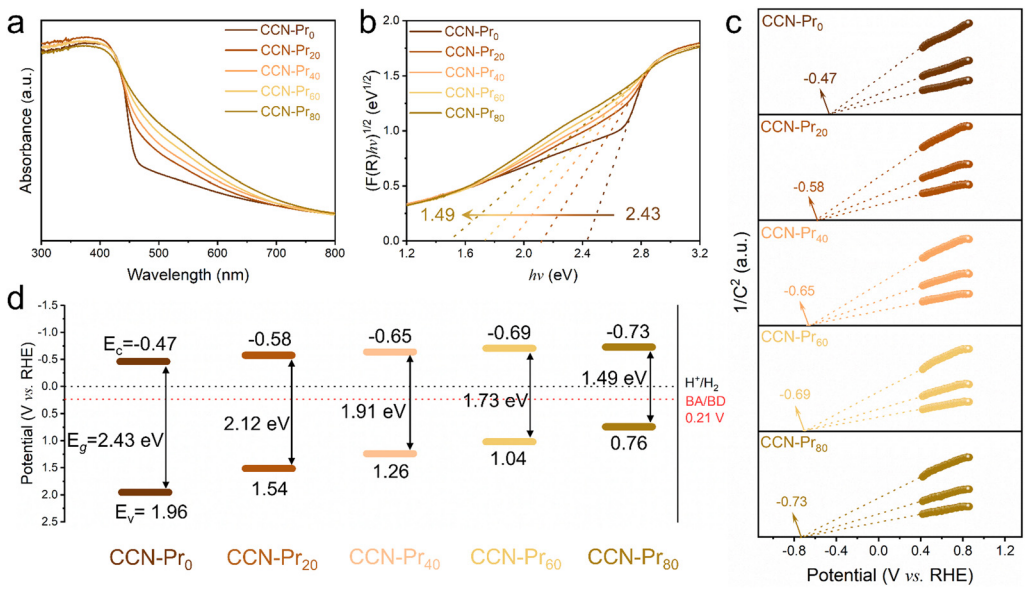

Fig. 3 (a) Ultraviolet-visible-near infrared diffuse reflectance spectra, (b) plots of the transformed Kubelka–Munk function *versus* photon energy, (c) Mott–Schottky plots and (d) band structures of CCN-Pr_x (x = 0, 20, 40, 60, 80). BA and BD represent benzyl alcohol and benzaldehyde, respectively.

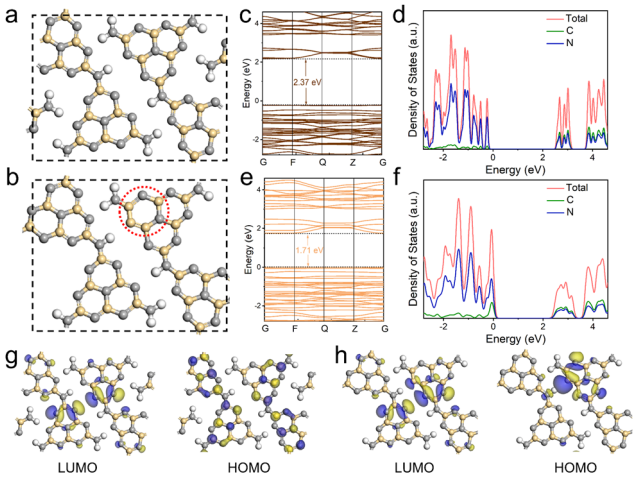

Fig. 4 Structure models of (a) CCN-Pr_0 and (b) CCN-Pr_{40}. Calculated band structures and corresponding DOS of (c and d) CCN-Pr_0 and (e and f) CCN-Pr_{40}. LUMO and HOMO distributions of (g) CCN-Pr_0 and (h) CCN-Pr_{40}. The blue and yellow regions represent the net electron accumulation and depletion, respectively. The gray, yellow, and white spheres represent the N, C, and H atoms, respectively.

density-functional theory (DFT) calculations were carried out for CCN-Pr_0 (Fig. 4a) and CCN-Pr_{40} (Fig. 4b). The band structures and density of states (DOS) calculation results demonstrate that both C 2p and N 2p orbitals contribute to the CB, while the VB is predominantly composed of N 2p orbitals for both CCN-Pr_0 and CCN-Pr_{40} (Fig. 4c–f). With pyrimidine rings introduced, the C 2p orbitals of the newly introduced pyrimidine-carbon atoms would participate in the formation of VB and significantly elevate the VB position to narrow the bandgap.[39] The theoretically calculated E_g is significantly decreased from 2.37 eV for CCN-Pr_0 to 1.71 eV for CCN-Pr_{40}, which agrees well with the extended optical absorption and measured E_g for CCN-Pr_x (Fig. 3a and b). Further investigation into the highest occupied molecular orbital (HOMO) and lowest unoccupied molecular orbital (LUMO) locations reveals that both LUMO and HOMO orbitals show symmetrical and overlapping distributions over heptazine rings (Fig. 4g). This is due to the high symmetry of the planar structure in CCN-Pr_0. In contrast, the electron localization occurs near the electron-donating pyrimidine-carbon atoms in CCN-Pr_{40} (Fig. 4h), which leads to the redistribution of charge density, thus inducing the internal electric field to promote exciton dissociation and accelerate charge transport.[40] Furthermore, this charge density redistribution would enable the separation of redox reactive sites, promoting charge carrier separation and suppressing back reactions, which is believed to benefit the photocatalytic activity.[41]

The above theoretical calculation results suggest that the introduced electron-rich pyrimidine rings could promote exciton dissociation and charge separation by inducing the charge density redistribution in CCN-Pr_x. To strengthen this deduction, XANES spectra were further recorded in dark and under illumination at the C K-edge and N K-edge to monitor the photoexcited electronic transitions (Fig. 5a) in CCN-Pr_0 and CCN-Pr_{40}. With the introduction of pyrimidine rings, CCN-Pr_{40} exhibits more distinct dark-irradiation intensity variations in both C K-edge and N K-edge spectra than CCN-Pr_0 (Fig. 5b). This demonstrates a more efficient electron transition from the

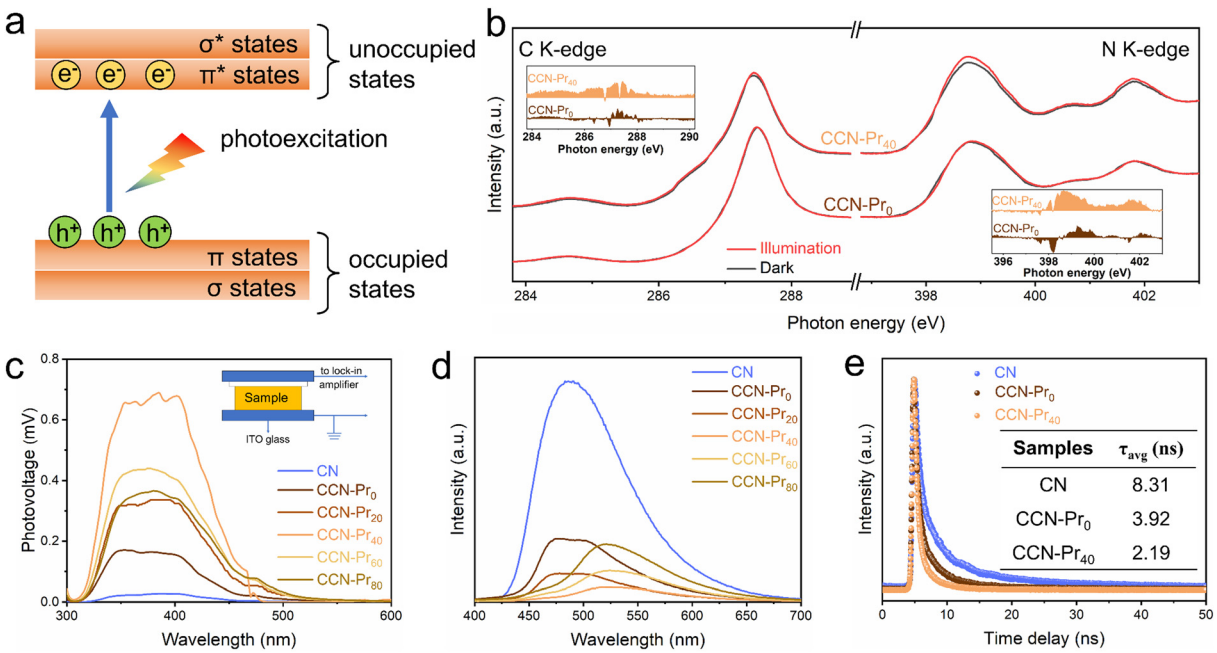

Fig. 5 (a) Illustration of the electron transition processes from the occupied states to unoccupied states in PCN. (b) C K-edge and N K-edge XANES spectra of CCN-Pr_0 and CCN-Pr_{40} with or without illumination. The inset in (b) exhibits the spectral difference between being in dark and illuminated conditions. (c) SPV and (d) steady-state PL emission spectra of CN and CCN-Pr_x. (e) Time-resolved transient PL decay spectra of CN, CCN-Pr_0 and CCN-Pr_{40}.

occupied states to unoccupied states in CCN-Pr_{40}.[42] This observation could be explained by the introduction of electron-rich pyrimidine rings that could induce the internal electric field to accelerate the exciton dissociation by the charge density redistribution over the PCN networks.[43] Moreover, the electron-rich pyrimidine rings would serve as the donor units to improve the charge separation and transfer by rapidly collecting photoexcited holes without recombination through the strong donor–acceptor interaction.[39] To further support the above deduction, the charge transfer property was then systematically investigated by surface photovoltage (SPV), photoluminescence (PL), and electron paramagnetic resonance (EPR) spectra. As monitored by SPV spectra (Fig. 5c), the positive SPV signals identify both CN and CCN-Pr_x with n-type semiconducting characteristic.[44] It should be noted that there are much stronger SPV signals observed for CCN-Pr_x than CN, meaning that the high crystallinity triggered by molten-salt annealing would favor photogenerated charge carrier separation. With electron-rich pyrimidine rings introduced, the SPV signals are gradually strengthened, reaching the maximum for CCN-Pr_{40}. These signals are then weakened, depending on the increasing TAP feeding amounts. This phenomenon suggests that the introduction of pyrimidine rings at an appropriate level is important to facilitate the separation of photogenerated charge carriers in CCN-Pr_x, which could be further confirmed by steady-state PL emission spectra. As shown in Fig. 5d, CN shows a strong PL emission peak, indicating the rapid charge carrier recombination,[17] while all the CCN-Pr_x samples exhibit significantly quenched PL emission, indicating the promoted charge carrier separation, as induced by the improved crystallinity of CCN-Pr_x. Specifically, the PL emission intensity first decreases and then increases, depending on the increasing TAP feeding amounts. The lowest PL intensity was attained for CCN-Pr_{40}, revealing the accelerated separation of photogenerated charge carriers in CCN-Pr_{40}. The improvement in charge carrier transfer ability could be also confirmed by the time-resolved transient PL decay spectra. As shown in Fig. 5e and Table S3 (ESI†), both CCN-Pr_0 (3.92 ns) and CCN-Pr_{40} (2.19 ns) exhibit much shorter average lifetimes (τ_{avg}) of photogenerated charge carriers with respect to CN (8.31 ns), suggesting that the high crystallinity triggered by molten-salt annealing is beneficial to accelerate the charge carrier transfer process. Moreover, the shortest average lifetime of the charge carriers in CCN-Pr_{40} again evidences that the introduction of electron-rich pyrimidine rings could remarkably promote photogenerated charge carrier separation and transfer.[15] These results are also supported by EPR analysis (Fig. S3, ESI†). It should be noted that all three samples, *i.e.*, CN, CCN-Pr_0, and CCN-Pr_{40}, exhibit an obvious Lorentzian line with g factor of 2.003, which is caused by the unpaired electrons on the π-conjugated aromatic rings.[17] In comparison to amorphous CN, CCN-Pr_0 exhibits a remarkably increased EPR signal, indicating that the high crystallinity triggered by molten-salt annealing would favor the delocalization of electrons on the aromatic heptane rings. Moreover, the much stronger EPR signal observed for CCN-Pr_{40} than CCN-Pr_0 means that the introduced electron-rich pyrimidine rings would provide more unpaired delocalized electrons in CCN-Pr_{40},[17] which is beneficial to promote the charge carrier separation.

The photocatalytic activity for hydrogen evolution over CCN-Pr_x was evaluated in an aqueous solution containing benzyl alcohol that was selectively oxidized to benzaldehyde. With the band and electronic structures well tuned by the introduction of electron-rich pyrimidine rings, the obtained CCN-Pr_x photocatalysts could effectively drive water reduction and benzyl alcohol oxidation relations for simultaneous and stoichiometric hydrogen and benzaldehyde evolution (Fig. 6a). All CCN-Pr_x (x = 0, 20, 40, 60, 80) samples with high crystallinity exhibit significantly increased photocatalytic hydrogen and benzaldehyde evolution rates, as compared to amorphous CN, which should be attributed to the improved light absorption (Fig. S4, ESI†) and the rapid charge carrier separation, benefiting from the high crystallinity triggered by molten salt annealing. Specifically, the photocatalytic activity increases first and then decreases for CCN-Pr_x, depending on the increasing contents of TAP fed in precursors. The highest hydrogen (149.39 μmol h^{-1}) and benzaldehyde (154.62 μmol h^{-1}) evolution rates are achieved over CCN-Pr_{40}, which are about 6.7 times those of CN (22.36 μmol h^{-1} and 17.22 μmol h^{-1}) and 2.2 times those of CCN-Pr_0 (68.65 μmol h^{-1} and 64.18 μmol h^{-1}), standing among the highest level reported for PCN-based photocatalysts (Table S4, ESI†). Considering that the introduction of pyrimidine rings does not significantly change the specific surface area (Fig. S5, ESI†), this volcano-shaped dependence of the photocatalytic activity on the TAP feeding amounts should be mainly attributed to the synergistically modulated band and electronic structures of CCN-Pr_x with introduced pyrimidine rings. With the introduced electron-rich pyrimidine rings, the VB position of CCN-Pr_x is gradually elevated to narrow the bandgap and extend the optical absorption (Fig. 3a and d). Meanwhile, the oxidation ability of the photogenerated holes gradually decreases with the elevating VB position,[45] leading to the weakened driving force for the benzyl alcohol oxidation reaction. It should be further noted that with the electron-rich pyrimidine rings introduced into CCN-Pr_x at a moderate level, the triggered charge density redistribution would benefit the efficient electron excitation and the promoted charge transport. However, the excessive pyrimidine rings in CCN-Pr_x would serve as the recombination sites for charge carriers, and thus retard the charge transfer and separation processes.[41] Therefore, CCN-Pr_{40} with synergistically engineered band and electronic structures exhibits the highest photocatalytic hydrogen and benzaldehyde evolution rates. This is due to the rapid charge carrier separation, the broadened optical absorption, and the well-tuned driving force for the benzyl alcohol oxidation reaction. CCN-Pr_{40} exhibits significantly improved conversion (91%) and selectivity (99%) for benzyl alcohol selective oxidation into benzaldehyde in a 12 hour reaction (Fig. 6b and Table S5, ESI†), with respect to CCN-Pr_0 (conversion: 73%; selectivity: 89%) and CN (conversion: 36%; selectivity: 89%). Encouragingly, solar-to-hydrogen (STH) and apparent quantum yield (AQY) were calculated to be as high as 0.74% under one-sun illumination (Fig. 6c and Table S6, ESI†) and 20.27% at 420 nm (Fig. 6d), respectively, which even outperforms the most previously reported PCN-based photocatalysts for hydrogen evolution in sacrificial reagent solutions (Table S7, ESI†). The optical

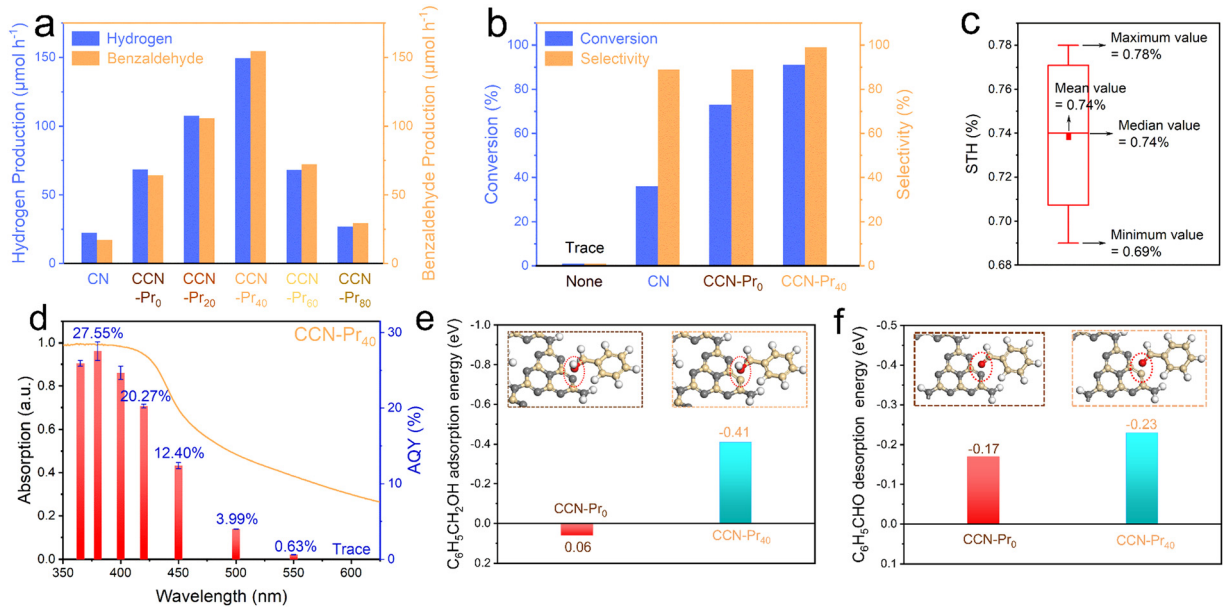

Fig. 6 (a) Hydrogen and benzaldehyde evolution rates for CN and CCN-Pr$_x$. (b) The benzyl alcohol conversion and benzaldehyde selectivity of CN, CCN-Pr$_0$ and CCN-Pr$_{40}$. (c) The STH of CCN-Pr$_{40}$ for photocatalytic hydrogen evolution in H_2O and benzyl alcohol solution. The STH value was evaluated 11 times with separate samples. (d) The wavelength-dependent AQY of the hydrogen evolution reaction over CCN-Pr$_{40}$. (e) Benzyl alcohol adsorption and (f) benzaldehyde desorption energies of CCN-Pr$_0$ and CCN-Pr$_{40}$. The gray, yellow, red and white spheres represent N, C, O and H atoms, respectively.

absorption profile closely dependent AQY values obtained for CCN-Pr$_{40}$ suggest that this hydrogen evolution reaction is indeed driven by photoexcitation, with hydrogen mainly produced *via* water reduction as confirmed by the D_2O isotope labeled photocatalytic measurement (Fig. S6, ESI†). A considerable activity could be still detected with the illumination wavelengths extended to be longer than 500 nm, indicating that the narrowed bandgap and the extended optical absorption greatly contribute to the improved photocatalytic activity of CCN-Pr$_{40}$. The photocatalytic hydrogen evolution activity could be well recovered by supplementing benzyl alcohol after reacting for an extended time (Fig. S7, ESI†). Furthermore, the chemical structure and composition of CCN-Pr$_{40}$ are well maintained before and after photocatalytic reaction (Fig. S8 and Table S8, ESI†), proving that CCN-Pr$_{40}$ is stable for photocatalytic hydrogen evolution coupled with benzyl alcohol selective oxidation.

By looking into the oxidation reaction for selective conversion of benzyl alcohol to benzaldehyde, the active sites were further theoretically identified to investigate the adsorption of benzyl alcohol molecules and the desorption of benzaldehyde molecules at the surface of CCN-Pr$_x$, which could be another determinant to the photocatalytic activity for simultaneous and stoichiometric hydrogen and benzaldehyde evolution. With computational configurations and adsorption energies of benzyl alcohol presented and calculated for CCN-Pr$_0$ and CCN-Pr$_{40}$ (Fig. 6e), one would note a positive adsorption energy (0.06 eV) required for the benzyl alcohol molecules to be adsorbed at N atoms in CCN-Pr$_0$, indicating that the adsorption and activation of benzyl alcohol at the N atoms of heptazine rings is unfavored. In contrast, the adsorption of energy required for benzyl alcohol molecules at the pyrimidine-carbon atoms of the introduced pyrimidine rings in CCN-Pr$_{40}$ is substantially reduced to −0.41 eV. Moreover, a more negative desorption energy of benzaldehyde is required for CCN-Pr$_{40}$ (−0.23 eV) than CCN-Pr$_0$ (−0.17 eV) (Fig. 6f), suggesting that the desorption of benzaldehyde on CCN-Pr$_{40}$ is easier than on CCN-Pr$_0$. Thus, the theoretical calculation results indicate that the pyrimidine-carbon atoms in pyrimidine rings could act as reactive sites that are superior to the N atoms in heptazine rings for benzyl alcohol adsorption and benzaldehyde desorption, thus accelerating the surface reaction kinetics for the selective oxidation of benzyl alcohol to benzaldehyde.[46]

Based on the above experimental characterization and theoretical calculation results, the significant improvement in the photocatalytic activity of CCN-Pr$_{40}$ for hydrogen evolution coupled with benzyl alcohol selective oxidation can be explained as follows: (1) The introduced electron-rich pyrimidine rings could finely tune the CB and VB positions to extend the optical absorption, with the redox potentials well matched to the water reduction and benzyl alcohol selective oxidation reactions. (2) The introduced electron-rich pyrimidine rings would trigger charge density redistribution for efficient electron excitation and promoted charge transport. (3) The C atoms in the electron-rich pyrimidine rings could serve as the reactive sites for the rapid adsorption of benzyl alcohol and desorption of benzaldehyde, and then accelerate the surface oxidation reaction kinetics (Fig. 7). These synergistic effects contributed from the tuned band and electronic structures give rise to the remarkable enhancement in photocatalytic benzyl alcohol oxidation and hydrogen evolution over PCN with molecular structures rationally engineered *via* the introduction of electron-rich pyrimidine rings.

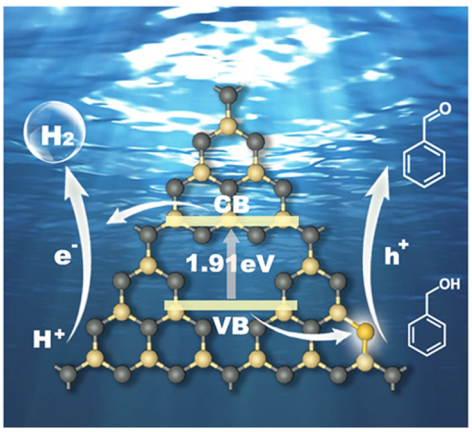

Fig. 7 Reaction mechanism of the photocatalytic hydrogen evolution coupled with benzyl alcohol oxidation for CCN-Pr_{40}. Yellow: C, gray: N.

Conclusion

In summary, high crystalline CCN-Pr with electron-rich pyrimidine rings introduced into the molecular structure was synthesized *via* two-step self-assembly and molten-salt annealing strategy. With molecular structures altered by the introduced pyrimidine rings, the obtained CCN-Pr exhibits significant improvement in photocatalytic activities for hydrogen evolution and benzyl alcohol selective oxidation, with the optimized hydrogen and benzaldehyde evolution rates reaching 149.39 μmol h^{-1} and 154.62 μmol h^{-1}. It is well evidenced that the band structures could be tuned successively *via* the introduction of electron-rich pyrimidine rings for the extended optical absorption and the matched redox potentials for water reduction and benzyl alcohol oxidation reactions. Furthermore, the introduced electron-rich pyrimidine rings would induce charge density redistribution for the promoted charge carrier transfer and separation. Meanwhile, the C atoms in the introduced pyrimidine rings could serve as the reactive sites for the rapid adsorption of benzyl alcohol and desorption of benzaldehyde, thus accelerating the surface oxidation reaction kinetics. This work provides a facile and reliable strategy to design novel and efficient PCN photocatalysts with band and electronic structures engineered by the tunable molecular structures, and also opens a new avenue for high performance and value-added solar energy conversion and utilization.

Author contributions

For author contributions, Z. Lin carried out the sample preparations, characterizations and photocatalytic measurements. Y. Wang, Z. Zhang, and D. Zhao conducted the DFT calculations. Z. Lin, J. Zhang and S. Shen wrote the paper. T. T. Thuy Nga and C.-L. Dong carried out the XAS measurements. R. Wang and Y. Xu detected the benzyl alcohol and benzaldehyde concentrations. S. Shen conceived the idea and supervised the project. All authors discussed the results and commented on the manuscript.

Conflicts of interest

There are no conflicts to declare.

Acknowledgements

The authors are thankful for the financial support from the National Natural Science Foundation of China (52225606, 51888103), the ''Fundamental Research Funds for the Central Universities'', and ''The Youth Innovation Team of Shaanxi Universities''.

Notes and references

1 X. Chen, S. Shen, L. Guo and S. S. Mao, Semiconductor-based Photocatalytic Hydrogen Generation, *Chem. Rev.*, 2010, **110**, 6503.
2 C. Bie, L. Wang and J. Yu, Challenges for photocatalytic overall water splitting, *Chem*, 2022, **8**, 1567–1574.
3 X. Tao, Y. Zhao, S. Wang, C. Li and R. Li, Recent advances and perspectives for solar-driven water splitting using particulate photocatalysts, *Chem. Soc. Rev.*, 2022, **51**, 3561–3608.
4 T. Banerjee, F. Podjaski, J. Kröger, B. P. Biswal and B. V. Lotsch, Polymer photocatalysts for solar-to-chemical energy conversion, *Nat. Rev. Mater.*, 2020, **6**, 168–190.
5 W. J. Ong, L. L. Tan, Y. H. Ng, S. T. Yong and S. P. Chai, Graphitic Carbon Nitride ($g\text{-}C_3N_4$)-Based Photocatalysts for Artificial Photosynthesis and Environmental Remediation: Are We a Step Closer To Achieving Sustainability?, *Chem. Rev.*, 2016, **116**, 7159.
6 B. Zhai, H. Li, G. Gao, Y. Wang, P. Niu, S. Wang and L. Li, A Crystalline Carbon Nitride Based Near-Infrared Active Photocatalyst, *Adv. Funct. Mater.*, 2022, **32**, 2207375.
7 L. Lin, Z. Lin, J. Zhang, X. Cai, W. Lin, Z. Yu and X. Wang, Molecular-level insights on the reactive facet of carbon nitride single crystals photocatalysing overall water splitting, *Nat. Catal.*, 2020, **3**, 649–655.
8 Y. Wang, D. Zhao, H. Deng, M. Li, J. Chen and S. Shen, Theoretical Insights into the Limitation of Photocatalytic Overall Water Splitting Performance of VIA Group Elements Doped Polymeric Carbon Nitride: A Density Functional Theory Calculation Predicting Solar-to-Hydrogen Efficiency, *Solar RRL*, 2021, **5**, 2000630.
9 B. Fang, Z. Xing, D. Sun, Z. Li and W. Zhou, Hollow semiconductor photocatalysts for solar energy conversion, *Adv. Powder Mater.*, 2022, **1**, 100021.
10 G. Zhang, G. Li, Z. A. Lan, L. Lin, A. Savateev, T. Heil, S. Zafeiratos, X. Wang and M. Antonietti, Optimizing Optical Absorption, Exciton Dissociation, and Charge Transfer of a Polymeric Carbon Nitride with Ultrahigh Solar Hydrogen Production Activity, *Angew. Chem., Int. Ed.*, 2017, **56**, 13445–13449.
11 X. Chen, J. Wang, Y. Chai, Z. Zhang and Y. Zhu, Efficient Photocatalytic Overall Water Splitting Induced by the Giant

Internal Electric Field of a g-C_3N_4/rGO/PDIP Z-Scheme Heterojunction, *Adv. Mater.*, 2021, **33**, 2007479.

12 D. Zhao, M. Wang, T. Kong, Y. Shang, X. Du, L. Guo and S. Shen, Electronic pump boosting photocatalytic hydrogen evolution over graphitic carbon nitride, *Mater. Today Chem.*, 2019, **11**, 296–302.

13 D. Zhao, X. Guan and S. Shen, Design of polymeric carbon nitride-based heterojunctions for photocatalytic water splitting: a review, *Environ. Chem. Lett.*, 2022, **20**, 3505–3523.

14 F. Chen, X. L. Wu, C. Shi, H. Lin, J. Chen, Y. Shi, S. Wang and X. Duan, Molecular Engineering toward Pyrrolic N-Rich M-N_4 (M = Cr, Mn, Fe, Co, Cu) Single-Atom Sites for Enhanced Heterogeneous Fenton-Like Reaction, *Adv. Funct. Mater.*, 2021, **31**, 2007877.

15 Z. Lin, Z. Zhang, Y. Wang, Z. Peng, X. Wang, R. Wang, Y.-C. Huang, F. Meng, M. Li, C.-L. Dong, Q. Zhang, L. Gu and S. Shen, Anchoring Single Nickel Atoms on Carbon-vacant Carbon Nitride Nanosheets for Efficient Photocatalytic Hydrogen Evolution, *Chem. Res. Chin. Univ.*, 2022, **38**, 1243–1250.

16 D. Zhao, Y. Wang, C.-L. Dong, Y.-C. Huang, J. Chen, F. Xue, S. Shen and L. Guo, Boron-doped nitrogen-deficient carbon nitride-based Z-scheme heterostructures for photocatalytic overall water splitting, *Nat. Energy*, 2021, **6**, 388–397.

17 Z. Lin, Y. Wang, Z. Peng, Y. C. Huang, F. Meng, J. L. Chen, C. L. Dong, Q. Zhang, R. Wang, D. Zhao, J. Chen, L. Gu and S. Shen, Single-Metal Atoms and Ultra-Small Clusters Manipulating Charge Carrier Migration in Polymeric Perylene Diimide for Efficient Photocatalytic Oxygen Production, *Adv. Energy Mater.*, 2022, **12**, 2200716.

18 A. Agosti, Y. Nakibli, L. Amirav and G. Bergamini, Photosynthetic H_2 generation and organic transformations with CdSe@CdS-Pt nanorods for highly efficient solar-to-chemical energy conversion, *Nano Energy*, 2020, **70**, 104510.

19 M. Y. Qi, M. Conte, M. Anpo, Z. R. Tang and Y. J. Xu, Cooperative Coupling of Oxidative Organic Synthesis and Hydrogen Production over Semiconductor-Based Photocatalysts, *Chem. Rev.*, 2021, **121**, 13051–13085.

20 M. J. Lima, A. M. T. Silva, C. G. Silva, J. L. Faria and N. M. Reis, Selective photocatalytic synthesis of benzaldehyde in microcapillaries with immobilized carbon nitride, *Chem. Eng. J.*, 2022, **430**, 132643.

21 J. Li, M. Li, H. Sun, Z. Ao, S. Wang and S. Liu, Understanding of the Oxidation Behavior of Benzyl Alcohol by Peroxymonosulfate via Carbon Nanotubes Activation, *ACS Catal.*, 2020, **10**, 3516–3525.

22 M. Tayyab, Y. Liu, S. Min, R. Muhammad Irfan, Q. Zhu, L. Zhou, J. Lei and J. Zhang, Simultaneous hydrogen production with the selective oxidation of benzyl alcohol to benzaldehyde by a noble-metal-free photocatalyst VC/CdS nanowires, *Chin. J. Catal.*, 2022, **43**, 1165–1175.

23 B. Wu, L. Zhang, B. Jiang, Q. Li, C. Tian, Y. Xie, W. Li and H. Fu, Ultrathin Porous Carbon Nitride Bundles with an Adjustable Energy Band Structure toward Simultaneous Solar Photocatalytic Water Splitting and Selective Phenylcarbinol Oxidation, *Angew. Chem., Int. Ed.*, 2021, **60**, 4815–4822.

24 T. Huo, Q. Deng, F. Yu, G. Wang, Y. Xia, H. Li and W. Hou, Ion-Induced Synthesis of Crystalline Carbon Nitride Ultrathin Nanosheets from Mesoporous Melon for Efficient Photocatalytic Hydrogen Evolution with Synchronous Highly Selective Oxidation of Benzyl Alcohol, *ACS Appl. Mater. Interfaces*, 2022, **14**, 13419–13430.

25 L. Lin, H. Ou, Y. Zhang and X. Wang, Tri-s-triazine-Based Crystalline Graphitic Carbon Nitrides for Highly Efficient Hydrogen Evolution Photocatalysis, *ACS Catal.*, 2016, **6**, 3921–3931.

26 Y. Xu, X. He, H. Zhong, D. J. Singh, L. Zhang and R. Wang, Solid Salt Confinement Effect: An Effective Strategy to Fabricate High Crystalline Polymer Carbon Nitride for Enhanced Photocatalytic Hydrogen Evolution, *Appl. Catal., B*, 2019, **246**, 349–355.

27 Y. Li, Y. Wang, C. L. Dong, Y. C. Huang, J. Chen, Z. Zhang, F. Meng, Q. Zhang, Y. Huangfu, D. Zhao, L. Gu and S. Shen, Single-atom nickel terminating sp^2 and sp^3 nitride in polymeric carbon nitride for visible-light photocatalytic overall water splitting, *Chem. Sci.*, 2021, **12**, 3633–3643.

28 G. Zhang, Y. Xu, D. Yan, C. He, Y. Li, X. Ren, P. Zhang and H. Mi, Construction of K^+ Ion Gradient in Crystalline Carbon Nitride to Accelerate Exciton Dissociation and Charge Separation for Visible Light H_2 Production, *ACS Catal.*, 2021, **11**, 6995–7005.

29 Z. Yu, X. Yue, J. Fan and Q. Xiang, Crystalline Intramolecular Ternary Carbon Nitride Homojunction for Photocatalytic Hydrogen Evolution, *ACS Catal.*, 2022, **12**, 6345–6358.

30 X. Wang, J. Meng, X. Zhang, Y. Liu, M. Ren, Y. Yang and Y. Guo, Controllable Approach to Carbon-Deficient and Oxygen-Doped Graphitic Carbon Nitride: Robust Photocatalyst Against Recalcitrant Organic Pollutants and the Mechanism Insight, *Adv. Funct. Mater.*, 2021, **31**, 2010763.

31 X. Zhou, Y. Liu, Z. Jin, M. Huang, F. Zhou, J. Song, J. Qu, Y. J. Zeng, P. C. Qian and W. Y. Wong, Solar-Driven Hydrogen Generation Catalyzed by g-C_3N_4 with Poly(platinaynes) as Efficient Electron Donor at Low Platinum Content, *Adv. Sci.*, 2021, **8**, 2002465.

32 C. Qiu, Y. Xu, X. Fan, D. Xu, R. Tandiana, X. Ling, Y. Jiang, C. Liu, L. Yu, W. Chen and C. Su, Highly Crystalline K-Intercalated Polymeric Carbon Nitride for Visible-Light Photocatalytic Alkenes and Alkynes Deuterations, *Adv. Sci.*, 2019, **6**, 1801403.

33 D. Liu, C. Li, C. Zhao, Q. Zhao, T. Niu, L. Pan, P. Xu, F. Zhang, W. Wu and T. Ni, Facile synthesis of three-dimensional hollow porous carbon doped polymeric carbon nitride with highly efficient photocatalytic performance, *Chem. Eng. J.*, 2022, **438**, 135623.

34 Y. Xu, M. Fan, W. Yang, Y. Xiao, L. Zeng, X. Wu, Q. Xu, C. Su and Q. He, Homogeneous Carbon/Potassium-Incorporation Strategy for Synthesizing Red Polymeric Carbon Nitride Capable of Near-Infrared Photocatalytic H_2 Production, *Adv. Mater.*, 2021, **33**, 2101455.

35 Y. Jiang, S. Fang, C. Cao, E. Hong, L. Zeng, W. Yang, L. Huang and C. Yang, Enhanced light harvesting and

charge separation of carbon and oxygen co-doped carbon nitride as excellent photocatalyst for hydrogen evolution reaction, *J. Colloid Interface Sci.*, 2022, **612**, 367–376.

36 C. Ehlert, W. E. Unger and P. Saalfrank, C K-edge NEXAFS spectra of graphene with physical and chemical defects: a study based on density functional theory, *Phys. Chem. Chem. Phys.*, 2014, **16**, 14083–14095.

37 S. Chu, Y. Wang, Y. Guo, J. Feng, C. Wang, W. Luo, X. Fan and Z. Zou, Band Structure Engineering of Carbon Nitride: In Search of a Polymer Photocatalyst with High Photooxidation Property, *ACS Catal.*, 2013, **3**, 912–919.

38 Y. Wang, S. Gonell, U. R. Mathiyazhagan, Y. Liu, D. Wang, A. J. M. Miller and T. J. Meyer, Simultaneous Electrosynthesis of Syngas and an Aldehyde from CO_2 and an Alcohol by Molecular Electrocatalysis, *ACS Appl. Energy Mater.*, 2018, **2**, 97–101.

39 G. Zhang, Y. Xu, H. Mi, P. Zhang, H. Li and Y. Lu, Donor Bandgap Engineering without Sacrificing the Reduction Ability of Photogenerated Electrons in Crystalline Carbon Nitride, *ChemSusChem*, 2021, **14**, 4516–4524.

40 G. Zhang, Y. Xu, G. Liu, Y. Li, C. He, X. Ren, P. Zhang and H. Mi, Pyrimidine donor induced built-in electric field between melon chains in crystalline carbon nitride to facilitate excitons dissociation, *Chin. Chem. Lett.*, 2022, **34**, 107383.

41 D. Zhao, Y. Wang, C. L. Dong, F. Meng, Y. C. Huang, Q. Zhang, L. Gu, L. Liu and S. Shen, Electron-Deficient Zn-N_6 Configuration Enabling Polymeric Carbon Nitride for Visible-Light Photocatalytic Overall Water Splitting, *Nano-Micro Lett.*, 2022, **14**, 223.

42 D. Zhao, C. L. Dong, B. Wang, C. Chen, Y. C. Huang, Z. Diao, S. Li, L. Guo and S. Shen, Synergy of Dopants and Defects in Graphitic Carbon Nitride with Exceptionally Modulated Band Structures for Efficient Photocatalytic Oxygen Evolution, *Adv. Mater.*, 2019, **31**, 1903545.

43 S. Gao, S. Wan, J. Yu and S. Cao, Donor–Acceptor Modification of Carbon Nitride for Enhanced Photocatalytic Hydrogen Evolution, *Adv. Sustainable Syst.*, 2022, **7**, 2200130.

44 Z. Zhang, X. Chen, H. Zhang, W. Liu, W. Zhu and Y. Zhu, A Highly Crystalline Perylene Imide Polymer with the Robust Built-In Electric Field for Efficient Photocatalytic Water Oxidation, *Adv. Mater.*, 2020, **32**, 1907746.

45 J. Zhang, G. Zhang, X. Chen, S. Lin, L. Mohlmann, G. Dolega, G. Lipner, M. Antonietti, S. Blechert and X. Wang, Co-monomer control of carbon nitride semiconductors to optimize hydrogen evolution with visible light, *Angew. Chem., Int. Ed.*, 2012, **51**, 3183–3187.

46 Q. Yang, T. Wang, Z. Zheng, B. Xing, C. Li and B. Li, Constructing interfacial active sites in Ru/g-C_3N_{4-x} photocatalyst for boosting H_2 evolution coupled with selective benzyl-alcohol oxidation, *Appl. Catal., B*, 2022, **315**, 121575.